RSC Advances

PAPER

View Article Online
View Journal | View Issue

Cite this: *RSC Adv.*, 2025, **15**, 10365

Atomic-scale insights into mechanical properties of calcium silicate hydrates: role of hydrogen bond networks and bond order distributions†

Neng Li, *[a] Deyong Zhou,[a] Jieshuo Wan,[a] Zhongyong Zhang,[a] Fujie Jia,[c] Jiayuan Ye,[c] Xiao Zhi[b] and Wei Chen[a]

Received 6th March 2025
Accepted 26th March 2025

DOI: 10.1039/d5ra01607j

rsc.li/rsc-advances

Calcium silicate hydrate (CSH) serves a critical role in maintaining the structural integrity of buildings. However, the relationships between its mechanical properties and crystal structures remain unclear. In this study, density functional theory (DFT) was used to systematically analyze the mechanical properties of 33 CSH phases. The findings demonstrate a linear correlation between elastic modulus and crystal density. In addition, the partial bond order (PBO) of Ca–O bonds significantly affects the crystal density. This effect, together with the water content, determines the mechanical properties of CSH. Notably, the unique cage-like hydrogen bond network present in kenotobermorite-4O markedly enhances the interlayer cohesion, giving it superior mechanical properties to those of conventional CSH. Additionally, the study elucidates the anisotropic characteristics of CSH materials, revealing that mechanical anisotropy is strongly correlated with the enhancement of PBO(Ca–O). These findings offer a theoretical framework for comprehending the mechanical behavior of CSH and establishing essential connections between its microstructure and mechanical properties.

1 Introduction

As the primary hydration product of cement, CSH and its crystalline phases play crucial roles in nucleation induction,[1,2] heavy metal ion adsorption,[3,4] and CO_2 sequestration.[5]The structural characteristics of CSH critically influence the strength and durability of cement-based binding materials, making it imperative to further investigate the correlation between its structure and elastic properties.[6–9]

However, structural characterization through conventional experimental techniques faces inherent limitations.[10–12] Impurities in natural CSH minerals and the low crystallinity of synthetic CSH hinder the precise analysis of their mechanical behavior.[13–15] DFT calculations have gained growing recognition in cementitious materials research for overcoming micromechanical limitations through atomic-scale electronic structure analysis. Mai *et al.*[16] systematically studied cement clinker minerals using DFT, achieving elastic modulus values with less than 5% deviation from experimental results, thereby validating the method's reliability in calcium silicate systems. Chamila's[17–19] team employed bond order distribution analysis and density of states calculations to reveal, for the first time, the electronic-structure-driven mechanism of interlayer cohesion in CSH, achieving atomic-scale mechanical insights not possible through traditional experiments.

Beyond overcoming the limitations of crystallinity, DFT allows for the prediction of anisotropic elastic tensors through stress–strain simulations. This establishes a theoretical framework for understanding the mechanical anisotropy of CSH. These benefits are particularly evident in carbon-containing CSH analogues. For example, Gao *et al.*[20] simulated the structural evolution of spurrite and other calcium silicate carbonates under varying pressure conditions. Their research revealed how $[CO_3]^{2-}$ influence the compressibility of these minerals through electronic rearrangement. This ability to dynamically capture the reconstruction of chemical bonds during carbonation provides valuable theoretical guidance for designing low-carbon cementitious materials.

Current research on cementitious materials primarily focuses on the CSH phases proposed by Richardson.[21] While there are some studies investigating the mechanical properties of mineral phases within the $CaO–SiO_2–CO_2–H_2O$ system, significant gaps remain in our understanding of their elastic behaviour. This is largely due to the limited availability of natural mineral specimens and the challenges involved in synthetic preparation. Several CSH analogs,[22–25] such as pectolite, oyelite, and cuspidine, have been documented. However, their electronic structures and mechanical profiles remain

[a]State Key Laboratory of Silicate Materials for Architectures, Wuhan University of Technology, Wuhan 430070, China. E-mail: lineng@whut.edu.cn
[b]China National Building Material Group Co., Ltd, Beijing 100036, China
[c]State Key Laboratory of Green Building Materials, China Building Materials Academy, Beijing 100024, China

† Electronic supplementary information (ESI) available. See DOI: https://doi.org/10.1039/d5ra01607j

poorly characterised. Moreover, the elastic properties of recently identified natural CSH phases—including trabzonite, hydroxyledgrewite, and chegemite[26–28]—still lack systematic investigation, revealing critical unresolved questions in this field.

To tackle these challenges, this study uses DFT to systematically investigate 33 crystalline CSH phases and their analogues. The goal is to analyse the bond order distributions and mechanical properties of these materials in depth, revealing the intrinsic connections between the microstructure of cement-based materials and their macroscopic mechanical performance. These findings are intended to provide a theoretical foundation for designing new CSH materials and predicting their mechanical behavior.

2 Computational details

All calculations concerning the structural, elastic, and electronic properties were conducted using the Vienna *Ab initio* Simulation Package (VASP).[29,30] The electronic exchange-correlation energy is determined using the generalised gradient approximation of the Perdew–Burke–Ernzerhof scheme.[31] The projector augmented wave method[32] was used to describe the atomic pseudopotentials. In addition, the DFT-D3 dispersion correction was applied to account for van der Waals interactions.[33] The Brillouin zone is sampled using the Monkhorst–Pack mesh. The mesh size of the *k*-points is determined by the cell parameters of different CSH,[34,35] respectively. Geometry optimisation of all CSH was performed using total energy convergence tolerance of 10^{-6} eV per atom, maximum lattice point displacement within 10^{-3} Å, and maximum ionic Hellmann–Feynman force within 0.02 eV $Å^{-1}$. The conjugate-gradient method was employed for relaxing atomic geometries. The bond order calculations were carried out using the orthogonalized linear combination of atomic orbital (OLCAO) method.[36,37]

3 Results and discussion

3.1 Crystal structures of CSH

According to the CSH mineral classification proposed by Richardson[21] and Biagioni,[38] the known CSH phases have been systematically integrated and categorized based on their elemental composition. The tobermorite supergroup and jennite are classified as group a. Other CSH crystals containing Ca, Si, O, and H are classified as group b. Group c is characterized by wollastonite, kilchoanite, and katoite hydrogarnet. Group d consists of compounds that belong to the $CaO–SiO_2–CO_2–H_2O$ system. Lastly, group e includes all other mineral phases that do not fit into the previous groups.

The unit cell parameters before optimisation are provided in Table S1,† while Table S2† presents the optimised unit cell parameters and the volume change rate relative to the experimental values. After optimization, the changes in unit cell volumes were within 5%, indicating the high reliability of the results. Most of the crystals experienced expansion after optimization, with oyelite showing the most significant increase in unit cell volume at an expansion rate of 4.66%. Conversely, the nekoite exhibited the most significant volume reduction, recorded at −2.51%.

Fig. 1 illustrates the crystal structures of the various minerals involved in the calculations. It is important to note that this figure does not include some crystal structures of CSH that have been studied by Chamila *et al.* As illustrated in Fig. 1, minerals classified within group a, such as the tobermorite group and jennite, belong to the isosilicate category. The calcium polyhedra are predominantly represented as $[CaO_6]$ and $[CaO_7]$. Both riversideite and plombièrite-2M exhibit a single-chain structure. In contrast, other minerals demonstrate a double chain configuration, where silicon–oxygen chains run parallel to the layers of calcium polyhedra. Hydrogen bonds from hydroxyl and water molecules connect calcium polyhedron layers. Additionally, riversideite, tobermorite-2M, and plombièrite-2M contain 'zeolitic' calcium. This feature is absent in clinotobermorite and kenotobermorite polytype. In group b, which includes trabzonite, three silicate tetrahedra link together to form dreierketten chains, classifying them as sorosilicates.

In contrast, hydroxyledgrewite and chegemite consist of individual silicate tetrahedra, classifying them as nesosilicates.

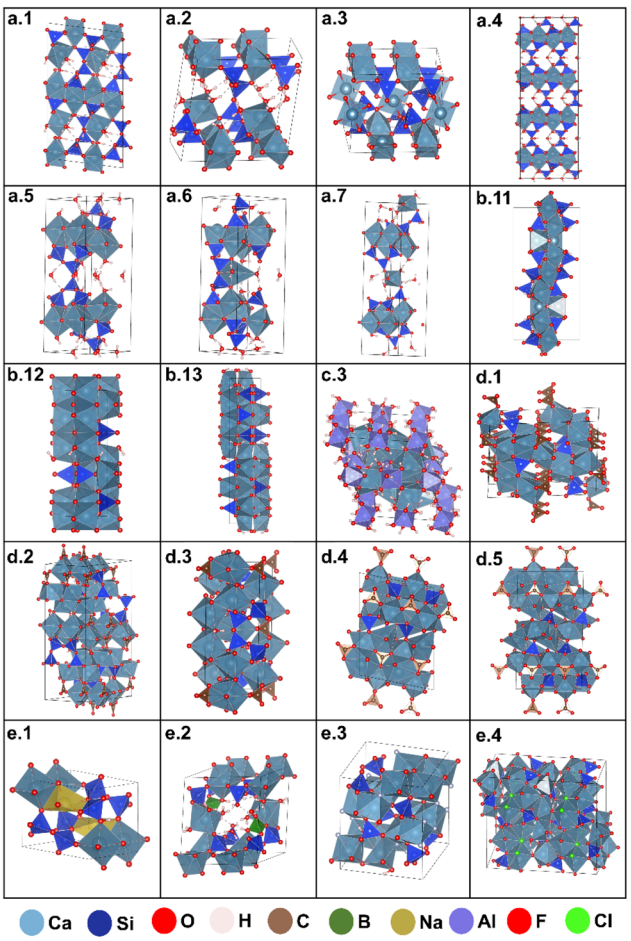

Fig. 1 Crystal structures of different CSH groups.

Due to their high calcium-to-silicon ratio, the three types of CSH structures have more complex calcium polyhedra compared to layered CSH. There are significant differences among the minerals in group d. The structure of katoite, a type of hydrogarnet, is primarily composed of isolated [AlO_6] polyhedra that are interconnected through calcium polyhedra. The minerals in group d differ considerably due to variations in their crystal formation conditions. However, since they all belong to the $CaO–SiO_2–CO_2–H_2O$ system, they share the presence of isolated carbonate groups. In the case of tilleyite, two silicate tetrahedra are linked in pairs, while fukalite features silicate tetrahedron chains. Scawtite is distinct with its cyclic structure, made up of six silicate tetrahedra, classifying it as a cyclosilicate. Both spurrite and galuskinite contain isolated silicate tetrahedra. For group e, pectolite and oyelite contain chain-like arrangements of silicate tetrahedra, with oyelite also featuring paired silicate tetrahedra. Cuspidine consists of isolated silicate tetrahedra, while rustumite features paired silicate tetrahedra, classifying it as a sorosilicate.

The presence of H_2O molecules or OH^- groups in these crystal structures is also noteworthy. With the exception of wollastonite, kilchoanite, tilleyite, spurrite, and galuskinite, all remaining structures contain H_2O, OH^-, or both. In group a, riversideite exhibits OH^- on calcium oxygen polyhedra. Both types of clinotobermorite contain water molecules between calcium oxygen layers or adsorbed on calcium oxygen polyhedra, Additionally, there are OH^- on calcium–oxygen polyhedra in other crystals. Xonotlite, calcium chondrodite, α-C_2SH, dellaite, jaffeite, rosenhahnite, fukalite, pectolite, cuspidine, rustumite, trabzonite, hydroxyledgrewite, and chegemite only have OH^- around calcium oxygen polyhedra. Katoite hydrogarnet has OH^- around Al and Ca atoms, forming $Al(OH)_6$ and $Ca(OH)_8$. Nekoite and scawtite only contain water molecules, while afwillite and suolunite have both OH^- and H_2O around calcium oxygen polyhedra. In oyelite, water molecules are concentrated between layers or adsorbed on calcium oxygen polyhedra, with OH^- combined on [BO_4].

3.2 Mechanical properties of CSH

The mechanical properties, including the bulk modulus (B), shear modulus (G), and Young's modulus (E), for the crystalline phases of 33 CSH are derived from the stiffness matrix (C_{ij}) calculated using VASP, as outlined in ESI.† The calculated elastic constants are listed in Table S3.† Determining mechanical stability and stiffness against external loads is a crucial aspect of the elastic constants of compounds. According to the Borne–Huang criterion, the mechanical stability of a crystal structure can be justified by the elastic constants.[39] All the elastic constants of CSH satisfy these mechanical stability criteria. This indicates that these phases are mechanically stable.

Table 1 summarizes the mechanical properties of the studied crystals, highlighting significant variations among them. Cuspidine exhibits the highest bulk modulus at 112.6 GPa and shear modulus at 63.9 GPa, demonstrating superior resistance to volumetric compression and shear deformation. In contrast, plombièrite-2M shows the lowest bulk modulus at 44.4 GPa and shear modulus at 20.7 GPa, indicating reduced structural stability under mechanical stress. Young's modulus ranges from 53.8 GPa for plombièrite-2M to 161.2 GPa for cuspidine, with cuspidine's exceptionally high value emphasizing its enhanced load-bearing capacity. These results position cuspidine as the most mechanically robust compound among those studied.

Table 1 Bulk modulus (*B*), shear modulus (*G*), Young's modulus (*E*), poisson's ratio of 33 crystal phases

Table	Phase	*B* (GPa)	*G* (GPa)	*E* (GPa)	Poisson's ration
a.1	Clinotobermorite-2M	73.5	34.5	89.4	0.297
a.2	Clinotobermorite-1A	100.7	50.7	130.3	0.284
a.3	Riversideite	96.9	54.6	138.0	0.263
a.4	Kenotobermorite-4O	95.4	58.6	145.9	0.245
a.5	Kenotobermorite-2M	70.4	32.5	84.5	0.300
a.6	Tobermorite-2M	57.5	28.5	73.4	0.287
a.7	Plombièrite-2M	44.4	20.7	53.8	0.298
a.8	Jennite	62.2	32.2	82.3	0.280
b.1	Foshagite	61.3	40.1	98.7	0.232
b.2	Nekoite	58.1	24.5	64.3	0.315
b.3	Xonotlite	69.1	45.9	112.8	0.228
b.4	Calcium chondrodite	108.8	58.5	148.8	0.272
b.5	Afwillite	77.0	34.0	89.0	0.307
b.6	α-C_2SH	99.0	53.0	135.0	0.273
b.7	Dellaite	84.6	44.0	112.6	0.278
b.8	Jaffeite	69.3	35.9	91.9	0.279
b.9	Rosenhahnite	75.0	41.9	105.9	0.265
b.10	Suolunite	61.3	40.6	99.7	0.229
b.11	Trabzonite	106.1	60.7	153.0	0.260
b.12	Hydroxyledgrewite	93.9	46.0	118.6	0.289
b.13	Chegemite	90.7	42.6	110.5	0.297
c.1	Wollastonite	80.4	42.0	107.2	0.278
c.2	Kilchoanite	108.6	62.4	157.1	0.259
c.3	Katoite hydrogarnet	59.0	30.4	77.9	0.280
d.1	Tilleyite	68.6	41.5	103.6	0.248
d.2	Fukalite	109.6	58.8	149.6	0.273
d.3	Scawtite	76.5	39.5	101.1	0.280
d.4	Spurrite	52.1	40.4	96.4	0.192
d.5	Galuskinite	79.7	43.2	109.7	0.270
e.1	Pectolite	85.1	47.3	119.8	0.265
e.2	Oyelite	59.1	35.8	89.3	0.248
e.3	Cuspidine	112.6	63.9	161.2	0.261
e.4	Rustumite	69.6	39.4	99.4	0.262

In the literature examining the elastic behaviour of CSH mineral phases, most studies have employed theoretical and computational methods to investigate this topic. Table 2 displays the mechanical properties of C–S–H phases reported in these studies. While the majority of the numerical values are closely aligned, some discrepancies arise due to variations in crystal structures. Additionally, a few results show more significant differences.

Fig. 2a–c illustrate the resistance strengths along three principal directions, indicating various distribution patterns. Fig. S1a–c† present the remaining elastic constants related to the materials' shear response. Fig. 2d reveals the correlation between Young's modulus and the density of CSH. Additionally,

Table 2 Comparison of bulk modulus values with previous work. Since molecular dynamics methods rely on force fields, the reference values provided only include experimental and DFT theoretical values, with bold representing experimental values

Table	Phase	Formula	Ref.	This work
a.1	Clinotobermorite-2M	$Ca_5Si_6O_{17}\cdot 5H_2O$	**93.5** (ref. 14)	73.5
a.2	Clinotobermorite-1A	$Ca_5Si_6O_{17}\cdot 5H_2O$	75.6 (ref. 40)	71.26
a.5	Kenotobermorite-2M	$Ca_4Si_6O_{15}(OH)_2\cdot 5H_2O$	**83.2**,[14] 67.7 (ref. 40)	70.4
a.6	Tobermorite-2M	$Ca_{4.5}Si_6O_{16}(OH)\cdot 5H_2O$	—	57.5
a.7	Plombièrite-2M	$Ca_5Si_6O_{16}(OH)_2\cdot 7H_2O$	**47**,[13] 49.3,[40] 46 (ref. 41)	44.4
a.8	Jennite	$Ca_9Si_6O_{18}(OH)6\cdot 8H_2O$	**64**,[15] 56.1,[40] 43 (ref. 41)	62.2
b.1	Foshagite	$Ca_4(Si_3O_9)(OH)_2$	73.6,[40] 74 (ref. 41)	61.3
b.2	Nekoite	$Ca_3Si_6O_{15}\cdot 7H_2O$	62.0,[40] 57 (ref. 41)	58.1
b.3	Xonotlite	$Ca_6Si_6O_{17}(OH)_2$	66 (ref. 42)	69.1
b.4	Calcium chondrodite	$Ca_5[SiO_4]_2(OH)_2$	82.3 (ref. 40)	108.8
b.5	Afwillite	$Ca_3(SiO_3OH)_2\cdot 2H_2O$	70.3 (ref. 40)	77.0
b.6	α-C_2SH	$Ca_2(HSiO_4)(OH)$	71.9 (ref. 40)	99.0
b.7	Dellaite	$Ca_6(Si_2O_7)(SiO_4)(OH)_2$	82.2 (ref. 40)	84.6
b.8	Jaffeite	$Ca_6[Si_2O_7](OH)_6$	66.1 (ref. 40)	69.3
b.9	Rosenhahnite	$Ca_3Si_3O_8(OH)_2$	76.2 (ref. 40)	75.0
b.10	Suolunite	$CaSiO_{2.5}(OH)\cdot 0.5H_2O$	75.3 (ref. 40)	61.3
c.1	Wollastonite	$Ca_3Si_3O_9$	92.6 (ref. 43)	80.4
c.2	Kilchoanite	$Ca_6(SiO_4)(Si_3O_{10})$	83.1 (ref. 40)	108.6
c.3	Katoite hydrogarnet	$Ca_3Al_2[OH]_{12}$	—	59.0
d.1	Tilleyite	$Ca_5Si_2O_7(CO_3)_2$	69.7 (ref. 20)	68.6
d.4	Spurrite	$Ca_5(SiO_4)_2(CO_3)$	77,[44] 71.1 (ref. 20)	52.1
d.5	Galuskinite	$Ca_7(SiO_4)_3(CO_3)$	75.0 (ref. 20)	79.7

Fig. S1d and e† show the relationship between both the bulk and shear modulus with density.

It is evident that there is a specific linear correlation between Young's modulus and density, with most values falling within a designated green area. Above this area, a blue region indicates CSH exhibiting a higher Young's modulus at the same density. The cell density plays a crucial role in determining the Young's modulus of CSH; as the cell density of the system increases, so does the modulus value of CSH. This finding is consistent with previous research, highlighting that the mechanical properties of CSH are intrinsically linked to its nanoscale structural evolution.

Interestingly, clinotobermorite-4O, a sample distinct from conventional CSH, demonstrates a significantly higher Young's modulus at a lower density compared to ordinary CSH. This unique property is further emphasized in Fig. 2e when contrasted with other materials.

Radar charts illustrating the mechanical properties of the CSH phases located in the blue area of Fig. 2d are shown in Fig. 3. The inclusion of kenotobermorite-4O (a4) and kenotobermorite-2M (a5), which are polytypes, allows for a comparative analysis of their mechanical characteristics using their respective radar charts. It is clear that the materials in this region generally exhibit high modulus values, consistent with the data presented in the previous table. Notably, cuspidine displays the highest modulus values among them.

When comparing kenotobermorite-4O to kenotobermorite-2M, kenotobermorite-4O demonstrates a significantly higher modulus and a lower Poisson's ratio than kenotobermorite-2M. This indicates that kenotobermorite-4O has greater stiffness, suggesting a more resilient structure when subjected to mechanical stress.

3.3 The role of bond order in the mechanical behavior of CSH

The bond order is a quantitative measure of the strength and stability of the bond between two atoms. By calculating the bond order, we can gain a deeper understanding of the bonding properties within the phases of CSH. This metric is handy for analyzing the complexities of interatomic bonding in materials like CSH, as it provides a clearer insight into the interactions involved.

The OLCAO calculations indicate that Si–O bonds, Ca–O bonds, O–H bonds, and hydrogen bonds primarily influence the bond order in the CSH phases. The Si–O bonds, originating from the $[SiO_4]$ tetrahedra, are a key feature of the CSH structure. These bonds typically exhibit a bond order between 0.25 and 0.35, with bond lengths around 1.65 Å, highlighting their strong covalent nature. In contrast, the Ca–O bonds, derived from $[CaO_6]$, $[CaO_7]$, and $[CaO_8]$ polyhedra, show greater variability in both bond lengths and bond order values. These bonds are generally longer, ranging from 2.28 to 3.0 Å, and have bond orders that span from 0.02 to 0.10, indicating a more ionic character compared to Si–O bonds. O–H bonds, influenced by the presence of H_2O and OH, have slightly lower bond orders, ranging from 0.24 to 0.28, with bond lengths around 1.0 Å. This reduction in bond order reflects the complex hydrogen bonding network present in CSH. Hydrogen bonds, which are generally weaker than O–H bonds, have bond lengths between 1.6 Å and 1.8 Å. They exhibit a bond order distribution from 0.02 to 0.10, with a typical range of approximately 0.02 to 0.08, similar to the distribution seen for Ca–O bonds.

The existence of multiple polytypes within the tobermorite species requires a detailed analysis of the bond order across the

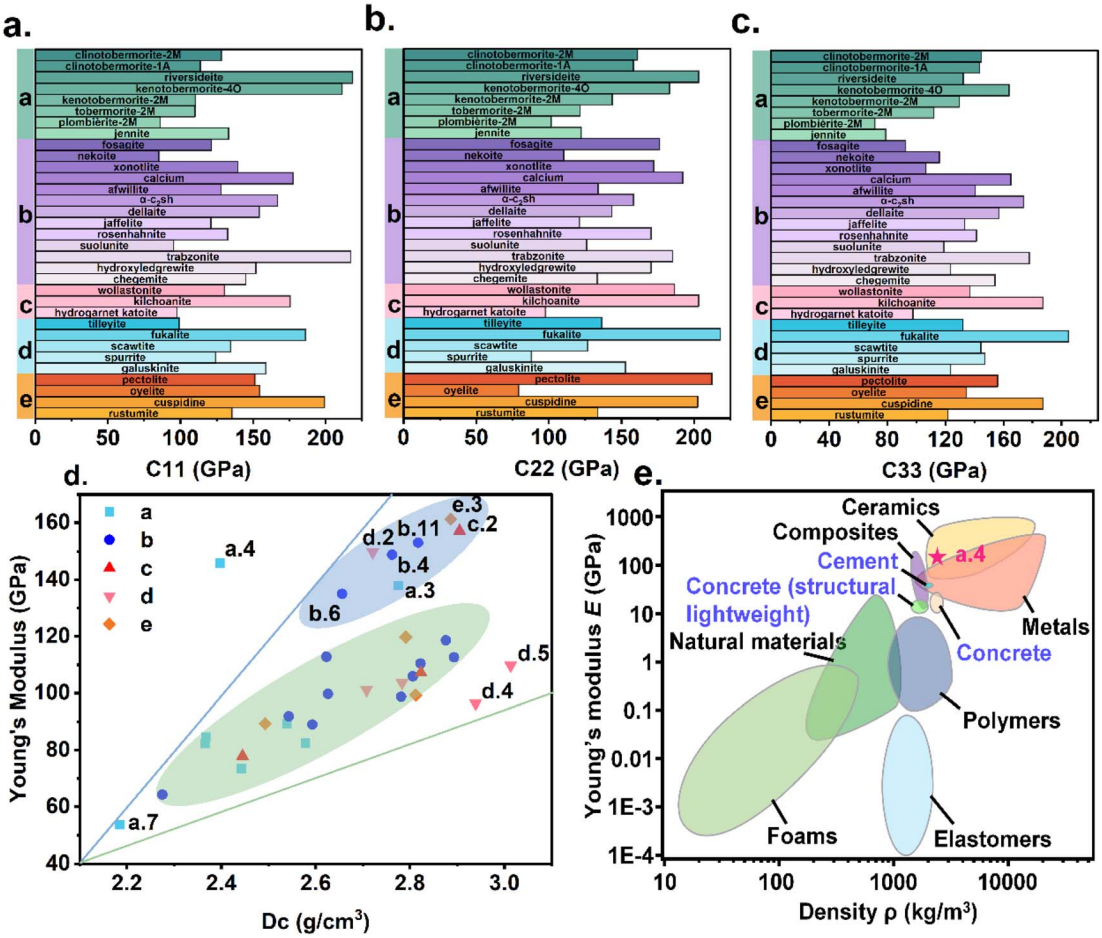

Fig. 2 (a–c) Distribution of C_{11}, C_{22}, and C_{33} values in CSH, (d) correlation analysis between Young's modulus (E) and density (D_c), and (e). Ashby diagram of Young's modulus E plotted against density ρ for different materials, including a.4. Reproduced from Ashby[45] with permission from Copyright 2005 Elsevier.

various tobermorite phases. Although these polytypes share the same chemical composition, their properties—especially bond order—can differ significantly due to variations in their space groups. Clinotobermorite-2M exhibits a bonding distribution similar to that of clinotobermorite-1A.

However, kenotobermorite-4O shows noticeable differences in its O–H and Ca–O bonds, as illustrated in Fig. S2.† Additionally, the Si–O and hydrogen bonds reveal significant variations between kenotobermorite-4O and kenotobermorite-2M. Kenotobermorite-4O has a concentration of Si–O bonds ranging from 0.25 to 0.30, while kenotobermorite-2M has a slightly broader range of 0.23 to 0.31, indicating that the Si–O bonds in kenotobermorite-2M are relatively weaker. The hydrogen bonding in kenotobermorite-4O is characterized by a significant number of bonds around 1.85 Å and a smaller quantity around 2.15 Å, with bond orders reaching as high as 0.033. In contrast, the hydrogen bonds in kenotobermorite-2M predominantly fall within the 2.0 Å range, with some observed at 2.1 Å, exhibiting bond orders between approximately 0.01 and 0.018. This variability is also reflected in the bond content illustrated by the pie charts in Fig. S2c and d,† which show that the proportion of hydrogen bonds in the total bond order of kenotobermorite-4O is considerably higher than that of kenotobermorite-2M. Despite sharing the identical chemical composition of $Ca_4Si_6O_{15}(OH)_2 \cdot 5H_2O$, these differences in bond formation—particularly in hydrogen bonds—are significant.

The bond order for the remaining tobermorite group minerals, including jennite, is presented in Fig. S3.† The analysis of these minerals shows a trend where an increase in water content correlates with a rise in O–H and hydrogen bonds. Simultaneously, there is a decrease in the number of Si–O bonds, indicating that hydration levels can significantly affect the bonding characteristics within the structure. Riversideite is particularly noteworthy for having the highest number of Si–O bonds among the group, highlighting the impact of water content on the bonding complexity. This variation in bond types and their prevalence contributes to the diversity in bond lengths and bond order values observed across the tobermorite group minerals. The analysis depicted in Fig. S3† for the tobermorite group minerals, including jennite, illuminates the complex interplay between water content and bonding characteristics, emphasizing the significant influence of hydration levels on the

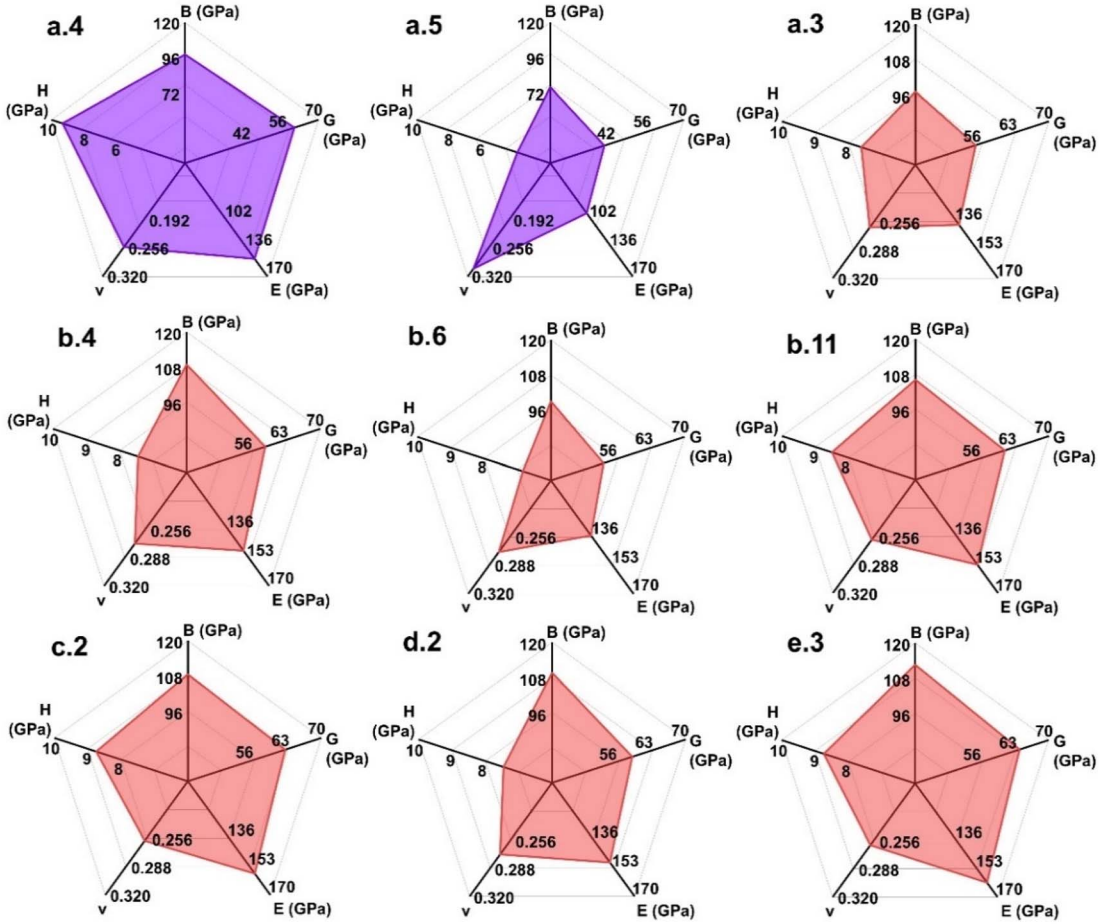

Fig. 3 Radar charts of the mechanical properties of CSH in blue area.

structural bond complexity. Importantly, the riversideite's high count of Si–O bonds highlights the diversity within this group.

This insight serves as a foundation for the examination in Fig. 4, which broadens the discussion to include trabzonite, hydroxyledgrewite, and chegemite, further exploring the bonding diversity among these CSH minerals. Trabzonite, for instance, presents a broader range of bond types, indicative of its enhanced structural complexity and varied polyhedral configurations. In contrast, hydroxyledgrewite and chegemite, characterised by their higher calcium content and the presence of discrete [SiO_4] tetrahedra, are classified as orthosilicates. Their bond order profiles are distinguished by a more significant contribution from Ca–O bonds, differentiating their bonding traits from those of trabzonite, a sorosilicate. Fig. 4d further elucidates these observations, mainly focusing on the unique bond order distribution of tilleyite. Tilleyite, a high-temperature formation product and a member of the sorosilicates, contains isolated carbonates within its structure. The bond order distribution of tilleyite indicates that the C–O bonds account for a substantial proportion, with bond lengths primarily at 1.35 Å and bond order peaking at 0.38 and 0.41. This suggests that the oxygen in the carbonate group likely diminishes the bond order of the C–O bond after interaction with calcium ions, a characteristic feature of the sorosilicate structure.

Consistent with the observations in Fig. S4,† scawtite stands out among carbonate-containing CSH analogs for having the lowest C–O bond order, with values ranging from 0.36 to 0.39. This is attributed to the co-prismatic linkage of carbonate ions with calcium–oxygen polyhedral in its structure. The shared oxygen atoms in these co-prismatic connections lead to electron delocalization between calcium and carbon, which weakens the C–O bonds and results in a lower bond order for scawtite than other mineral phases. Scawtite also exhibits the most enormous contribution from Si–O bonds, accounting for 55.9% of the total bond order. This is due to the high silicon content and the formation of [Si_6O_{18}] six-membered rings by [SiO_4] tetrahedra.

In contrast, fukalite, which contains hydroxyl groups, significantly contributes to the O–H bond order distribution. Characterized by silicate single chains, fukalite's structure exhibits a distinct configuration compared to that of tilleyite. The increased angularity of the silicate chains in fukalite suggests that high temperatures may have rearranged the silica–oxygen tetrahedral chains within the silicates, shifting from the originally acute angles to a more angular configuration. This contrasts with the more typical hydration products like tobermorite.

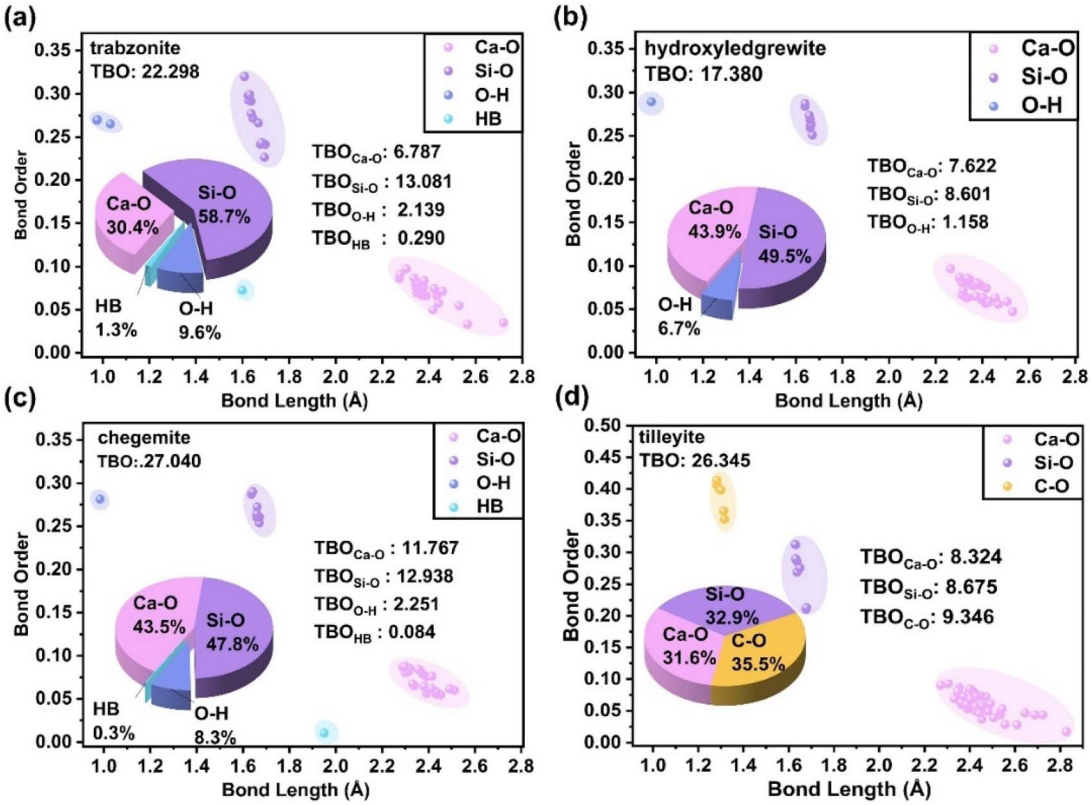

Fig. 4 Bond order of (a) trabzonite, (b) hydroxyledgrewite, (c) chegemite, and (d) tilleyite.

Spurrite and galuskinite, both orthosilicates, contain isolated carbonates within their structures. The Ca–O bond order distribution in these minerals is more complex than in scawtite or fukalite. This complexity stems from the presence of both [CaO_7] and [CaO_8] polyhedral in their structural systems, leading to a more intricate Ca–O bonding pattern. The coexistence of [SiO_4] and [CO_3^{2-}] monomers in these structures results in Ca–O bond order distributions that are highly similar between the two. This analysis offers a detailed view of the bonding characteristics and structural variations among these carbonate-containing CSH analogues, highlighting the influence of temperature and structural elements on their properties.

Pectolite's formation is characterized by the presence of [NaO_6] polyhedral resulting from Na (as shown in Fig. S5a†). Na–O bonds' bond order is concentrated between 0.2 and 0.9, which is within the same order of magnitude as that of Ca–O bonds. However, the overall distribution of Na–O bond order is lower, suggesting the predominantly ionic nature of these bonds within the pectolite structure. In the case of oyelite, the B–O bond lengths are concentrated around 1.5 Å, which is shorter than the typical Si–O (silicon–oxygen) bond length. This shorter bond length and a higher bond order bond order indicate a strong covalent character for the B–O bond. This covalent nature suggests that the B–O bond may serve as a structural backbone within the olivine system.

For cuspidine, partial substituting O with F leads to the formation of Ca–F bonds. These bonds have a range of 2.25 to 2.65 Å, which is comparable to the length of Ca–O bonds, but the bond order is concentrated in a lower range of 0.045. This indicates a weaker bonding interaction compared to the Ca–O bonds. The Ca–Cl (calcium–chlorine) bond in rustumite also exhibits ionic characteristics, with a bond order of approximately 0.05. However, the bond length of Ca–Cl is significantly larger, ranging from 2.8 to 3.0 Å, which is longer than that of the Ca–O bond. This increased bond length implies that Cl ions have a broader range of motion than O and F ions, reflecting the more ionic and less constrained nature of the Ca–Cl bond.

The correlation between bond order distributions and macroscopic properties in CSH systems reveals critical structure–property relationships. Table S4† summarizes PBO content of specific bonds, TBOD values, and H_2O wt% measurements. Fig. 5a demonstrates an inverse correlation between H_2O wt% and density, where water incorporation increases total mass but induces disproportionate volumetric expansion, ultimately reducing density.

Notably, c.3 katoite hydrogarnet, a calcium–aluminium hydrate without silicon, appears as an outlier in the figure, which may be related to its unique structure, thus showing a significant difference between calcium–aluminium and calcium–silicate cementitious materials. Fig. 5b shows the relationship between H_2O wt% and TBOD, and the data for katoite hydrogarnet is excluded from this analysis to minimise its impact on the results. The positive correlation trend indicates that as the water content increases, the TBOD value also increases, meaning that adding water molecules and hydroxyl

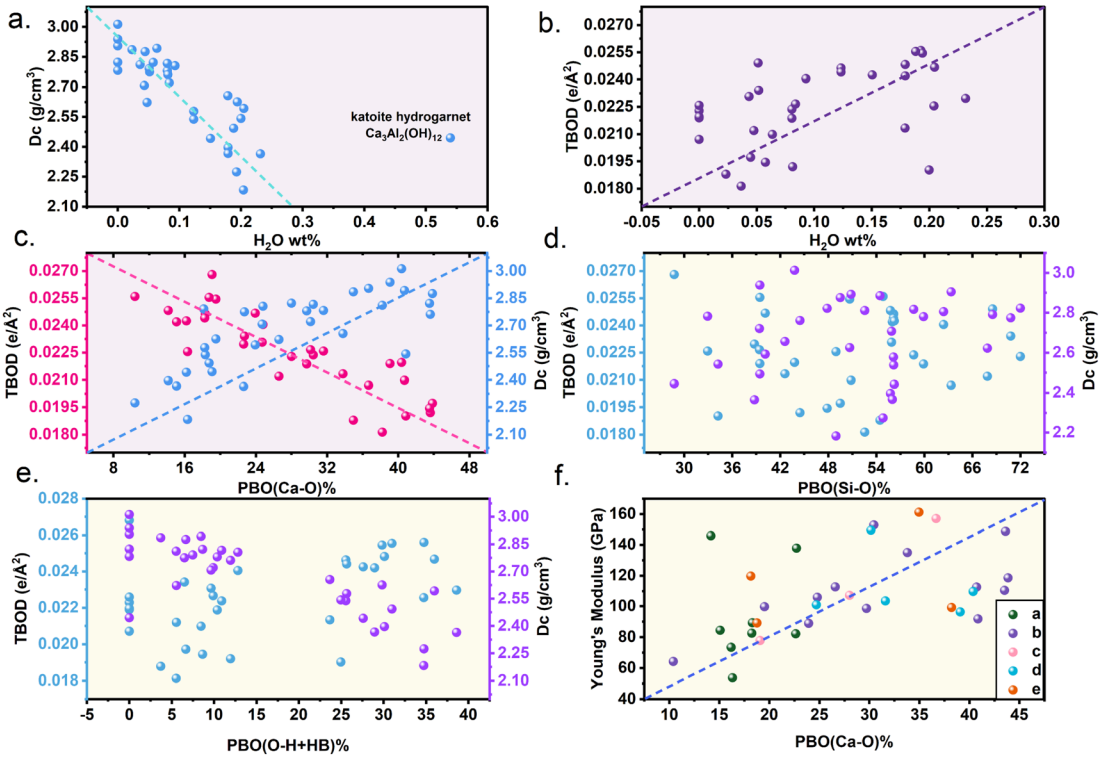

Fig. 5 (a) Variation of density with water content by mass percentage, (b) variation of total bond order density (TBOD) with water content by mass percentage, (c–e) changes in TBOD and density with PBO(Ca–O)%, PBO(Si–O)%, and PBO(O–H + HB)%, (f) distribution of Young's modulus (E in GPa) with PBO(Ca–O)%.

groups enhances the bond order density in the material, which may also lead to a decrease in density.

Fig. 5c further illustrates the relationship between TBOD and density with the percentage content of PBO(Ca–O). As the PBO(Ca–O) increases, the TBOD value decreases while the density value rises, suggesting that an increase in calcium–oxygen bonds reduces the TBOD in the material but helps form a more compact particle packing, thereby increasing density. Fig. 5d and e shows the relationship between TBOD and density with PBO(Si–O) and PBO(O–H + HB), respectively. The trends in these figures are more dispersed, with no clear correlation, indicating that in CSH, the content of water, hydroxyl groups, and calcium collectively affects the density of CSH.

As mentioned earlier, density has a decisive impact on the modulus value of the material, suggesting that an increase in TBOD may not directly lead to an increase in strength. Instead, the increase in density controlled by calcium–oxygen bonds helps form a more compact particle packing, which may improve the material's strength. Finally, Fig. 5f shows the relationship between PBO(Ca–O) and Young's modulus (GPa). The positive correlation trend indicates that as PBO(Ca–O) increases, Young's modulus also increases, meaning that an increase in calcium–oxygen bonds enhances the material's rigidity. This finding is of great significance for designing CSH-based materials with expected mechanical properties, and the synergistic effect of water, hydroxyl groups, and Ca–O may need to be given more attention.

3.4 Hydrogen bonding networks enhance the elastic modulus of CSH

Tobermorite, a pivotal phase in cement research, is crucial for elucidating the mechanical behaviour of cement gels. Building on this understanding, analysing specific CSH phases, particularly within the tobermorite supergroup, further clarifies how hydration levels and structural variations influence mechanical strength. Experimental data on the mechanical properties of certain minerals within the tobermorite supergroup, obtained through *in situ* synchrotron X-ray powder diffraction, indicate a bulk modulus of 83.2 GPa for kenotobermorite and 93.5 GPa for clinotobermorite.[14] Although it is common for the calculated properties of ideal CSH crystals to exceed experimental values, these figures are considerably higher than those reported in prior theoretical studies. While not perfectly aligned with experimental data, the mechanical properties reported in this study fall within an acceptable margin of error.

However, it is interesting to note a special case in the previous sections: a.4 kenotobermorite-4O, whose mechanical properties are significantly higher than those of another polytype, a.5 kenotobermorite-2M. The mechanical properties of CSH are controlled by density, yet kenotobermorite-4O shows a marked enhancement in its mechanical performance at a certain density. The reasons behind this deserve further exploration. This section aims to delve into the reasons behind the variations in mechanical properties observed among the different polytypes within the tobermorite supergroup,

particularly focusing on the fact that kenotobermorite-4O exhibits superior mechanical properties compared to kenotobermorite-2M.

There are notable differences in the hydrogen bonding networks (HBN) of kenotobermorite-4O and kenotobermorite-2M. The 4O structure features a cage-like arrangement where water molecules are interconnected by hydrogen bonds, creating a network that spans the spaces between calcium–oxygen polyhedral layers. Conversely, while the 2M structure has interlayer hydrogen bonding, it does not develop a network as extensive as that found in the 4O structure. The bond order values for hydrogen bonds, as illustrated in Fig. 6, support this observation. The cage-like HBN in the 4O structure contributes a significantly higher bond order, with the strongest bonds exceeding 0.03, which is markedly higher than any hydrogen bond in the 2M structure (as shown in Fig. 6d). This suggests that the 4O structure would have increased resistance along the (001) direction, which is consistent with the higher C_{33} value observed for the 4O structure compared to the 2M structure.

The HBN present in the 4O structure plays a pivotal role in bolstering the interlayer mechanical properties. Significantly, the 4O structure demonstrates superior values for the elastic constants C_{11} and C_{22}, as illustrated in the radar charts of Fig. 6g and h. In inosilicates, the (100) direction is often characterised by infinite silicate single or double chains, which are crucial for mechanical strength. In the 4O structure, between two silicate double chains along the (100) direction, there exists a hydrogen–oxygen chain linked by hydrogen bonds, shown in Fig. 6c, indicating that the cage-like hydrogen bonding network interacts synergistically with the silicate chains, further increasing resistance in this direction. The presence of the HBN between silicate double chains in the (010) direction also contributes to the mechanical strength. This explains the higher C_{11}, C_{22}, and C_{33} values in the 4O structure compared to the 2M structure. The cage-like HBN, with its higher bond order, is significantly stronger than isolated hydrogen bonds, and its presence within the structure can markedly improve the mechanical strength of CSH. This may offer a novel perspective: under a specific cell density, modulating the formation of HBN within CSH can contribute to developing materials with enhanced mechanical properties, making them lightweight and high-strength.

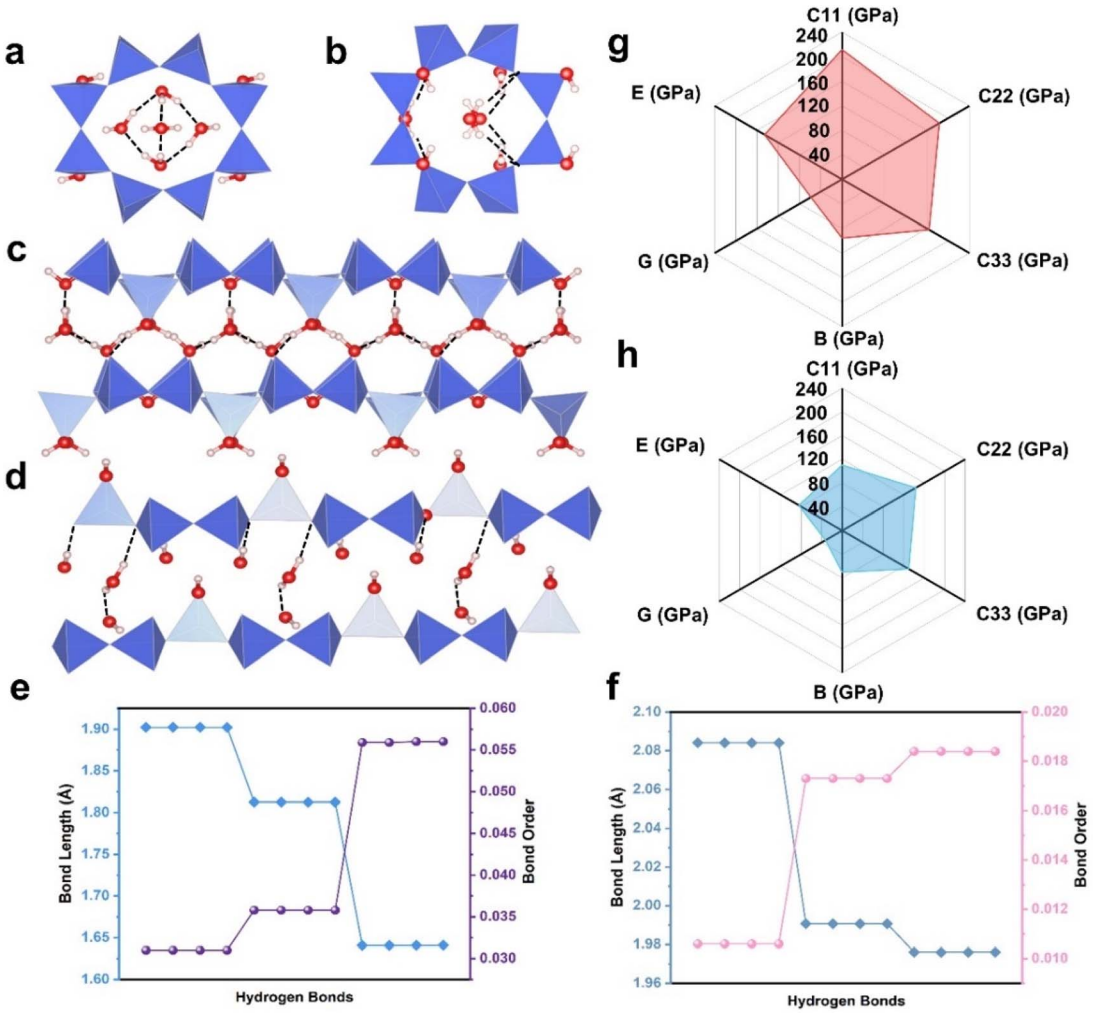

Fig. 6 Hydrogen bonding network in kenotobermorite. (a and c) The distribution of HBN in the 4O, (b and d). The distribution of HBN in the 2M, (e and f). The distribution of bond orders and lengths in 4O and 2M, (g and h). The radar chart of elastic constants and modulus in 4O and 2M.

3.5 Mechanical anisotropy of CSH

A three-dimensional representation of the material's anisotropy has been constructed to delve deeper into CSH's mechanical anisotropy. As previously discussed, the percentage of PBO(Ca–O) significantly influences the density of CSH materials, which in turn dictates their mechanical properties. Due to article length constraints, only the anisotropic distribution of Young's modulus in three-dimensional space is presented here, as shown in Fig. 7, S9, and S10,† with the corresponding PBO(Ca–O) values listed for the materials. In group a, most materials exhibit varying degrees of anisotropy, particularly pronounced in the tobermorite family of minerals. These materials demonstrate higher mechanical strength along the (100) and (010) crystal planes, while they are relatively weaker along the (001) plane. Notably, riversideite with the lowest water content, has the highest upper limit of Young's Modulus at 190 GPa. Conversely, plombièrite-2M with the highest water content, possesses the lowest limit of Young's Modulus at 20 GPa.

It is also observed that riversideite, kenotobermorite-4O and jennite exhibit a more uniform distribution of Young's Modulus. Additionally, a. three and a. eight are noted for their higher PBO(Ca–O). For kenotobermorite-4O, as discussed earlier, a strong HBN contributes to its mechanical uniformity. Analysis of three-dimensional anisotropy diagrams across different CSH systems reveals a strong dependence of mechanical anisotropy on PBO(Ca–O) characteristics. As the PBO(Ca–O) value of CSH increases, its three-dimensional anisotropy diagram gradually approaches a circular shape (Fig. 7e), and both E_max and E_min are significantly reduced.

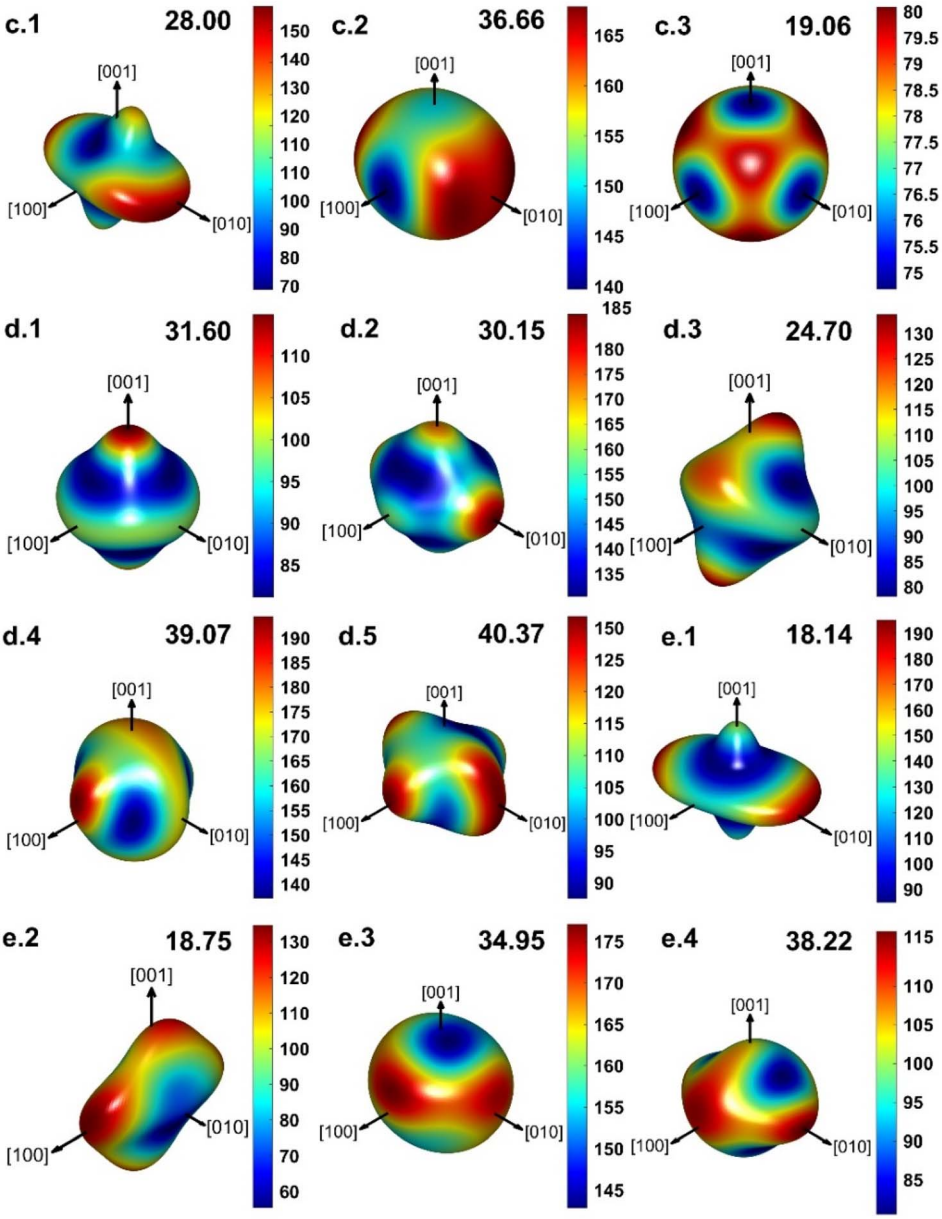

Fig. 7 Three-dimensional diagrams of Young's modulus of groups c, d, e.

This phenomenon indicates that a higher PBO(Ca–O) not only enhances the unit density by strengthening the calcium–oxygen bond network but more importantly, may induce structural ordering at the atomic scale—the orientation distribution between calcium silicate layers becomes more consistent, and the interlayer defect density is reduced, thereby diminishing the directional dependence of mechanical properties. This structural regulation effect provides a new approach for designing isotropic CSH-based composite materials. By precisely controlling the PBO(Ca–O) ratio, it is possible to achieve a wide-range tunable performance from highly anisotropic to quasi-isotropic.

4 Conclusions

This study employs DFT to systematically investigate the bond order distribution, mechanical properties, and anisotropy of 33 CSH and related phases. The key findings are summarized as follows:

(1) A linear correlation exists between the elastic modulus of CSH materials and their crystalline density. Increasing the PBO(Ca–O) enhances density by promoting denser particle packing, albeit reducing the TBOD. Conversely, higher water content elevates TBOD but lowers density.

(2) Kenotobermorite-4O exhibits superior mechanical properties compared to other polytypes, attributed to its unique cage-like HBN. This HBN reinforces interlayer cohesion and structural integrity, significantly improving Young's modulus. By controlling HBN formation at an optimal density, lightweight yet high-strength CSH materials can be engineered.

(3) CSH phases with higher PBO(Ca–O) demonstrate reduced mechanical anisotropy, approaching quasi-isotropic behavior. This uniformity stems from Ca–O bond-induced structural ordering, which minimizes interlayer defects and directional dependency. Such insights provide a foundation for designing CSH composites with tunable mechanical performance.

In summary, this work establishes a robust linkage between the microstructure (bond order, HBN, and density) and macroscopic mechanical properties of CSH materials, offering critical guidance for predicting their behavior in practical applications and advancing high-performance cementitious material design.

Data availability

The data that support the findings of this study are available from the corresponding author, Prof. Dr Neng Li (lineng@whut.edu.cn), upon reasonable request.

Conflicts of interest

There are no conflicts to declare.

Acknowledgements

This work was supported by the Key Technologies R&D Program of CNBM (No. 2021YCJS01-2), the National Key Research and Development Plan of China (No. 2019YFC1904900).

References

1 E. John, T. Matschei and D. Stephan, Nucleation Seeding with Calcium Silicate Hydrate – A Review, *Cem. Concr. Res.*, 2018, **113**, 74–85.
2 A. Cuesta, A. Morales-Cantero, A. G. De La Torre and M. A. G. Aranda, Recent Advances in C–S–H Nucleation Seeding for Improving Cement Performances, *Materials*, 2023, **16**(4), 1462.
3 J. Bu, R. Gonzalez Teresa, K. G. Brown and F. Sanchez, Adsorption Mechanisms of Cesium at Calcium–Silicate–Hydrate Surfaces Using Molecular Dynamics Simulations, *J. Nucl. Mater.*, 2019, **515**, 35–51.
4 K. Cui, X. Han, P. Zhou, M. Hao, X. Wang, L. Bian, J. Nie, G. Yang, J. Liang, X. Liu and F. Wang, A Novel Highly Dispersed Calcium Silicate Hydrate Nanosheets for Efficient High-Concentration Cu^{2+} Adsorption, *J. Hazard. Mater.*, 2024, **475**, 134774.
5 Y.-Q. Zhang, A. V. Radha and A. Navrotsky, Thermochemistry of Two Calcium Silicate Carbonate Minerals: Scawtite, $Ca_7(Si_6O_{18})(CO_3)\cdot 2H_2O$, and Spurrite, $Ca_5(SiO_4)_2(CO_3)$, *Geochim. Cosmochim. Acta*, 2013, **115**, 92–99.
6 R. Alizadeh, J. J. Beaudoin and L. Raki, Mechanical Properties of Calcium Silicate Hydrates, *Mater. Struct.*, 2011, **44**(1), 13–28.
7 L. Wang, H. Q. Yang, S. H. Zhou, E. Chen and S. W. Tang, Hydration, Mechanical Property and C–S–H Structure of Early-Strength Low-Heat Cement-Based Materials, *Mater. Lett.*, 2018, **217**, 151–154.
8 M. Youssef, R. J.-M. Pellenq and B. Yildiz, Glassy Nature of Water in an Ultraconfining Disordered Material: The Case of Calcium–Silicate–Hydrate, *J. Am. Chem. Soc.*, 2011, **133**(8), 2499–2510.
9 A. J. Allen, J. J. Thomas and H. M. Jennings, Composition and Density of Nanoscale Calcium–Silicate–Hydrate in Cement, *Nat. Mater.*, 2007, **6**(4), 311–316.
10 S. Zhu, H. Xu, M. S. Khan, M. Xia, F. Wang and Y. Chen, Enhanced Removal of Ni^{2+} and Co^{2+} from Wastewater Using a Novel 2-Hydroxyphosphonoacetic Acid Modified Mg/Fe-LDH Composite Adsorbent, *Water Res.*, 2025, **272**, 122997.
11 X. Wang, M. A. Khan, M. Xia, S. Zhu, W. Lei and F. Wang, Synthesis of RGO and G-C_3N_4 Hybrid with WO_3/Bi_2WO_6 to Boost Degradation of Nitroguanidine under Visible Light Irradiation, *J. Mater. Sci.: Mater. Electron.*, 2019, **30**(6), 5503–5515.
12 Z. Bano, N. Z. Ali, M. A. Khan, S. Mutahir, S. Zhu, F. Wang and M. Xia, Synthesis, characterization and applications of 3D porous graphene hierarchical structure by direct carbonization of maleic acid, *Ceram. Int.*, 2022, **48**(6), 8409–8416.
13 J. E. Oh, S. M. Clark, H.-R. Wenk and P. J. M. Monteiro, Experimental Determination of Bulk Modulus of 14 Å Tobermorite Using High Pressure Synchrotron X-Ray Diffraction, *Cem. Concr. Res.*, 2012, **42**(2), 397–403.

14 M. Polisi, M. G. Vezzalini, E. Bonaccorsi, C. Biagioni and R. Arletti, High Pressure Behaviour of Tobermorite Supergroup Minerals: An in Situ Synchrotron X-Ray Powder Diffraction Study, *Cem. Concr. Res.*, 2020, **138**, 106249.

15 J. Moon, S. Yoon and P. J. M. Monteiro, Mechanical Properties of Jennite: A Theoretical and Experimental Study, *Cem. Concr. Res.*, 2015, **71**, 106–114.

16 N. L. Mai, N.-H. Hoang, H. T. Do, M. Pilz and T. T. Trinh, Elastic and Thermodynamic Properties of the Major Clinker Phases of Portland Cement: Insights from First Principles Calculations, *Constr. Build. Mater.*, 2021, **287**, 122873.

17 C. C. Dharmawardhana, A. Misra and W.-Y. Ching, Quantum Mechanical Metric for Internal Cohesion in Cement Crystals, *Sci. Rep.*, 2014, **4**(1), 7332.

18 C. C. Dharmawardhana, A. Misra, S. Aryal, P. Rulis and W. Y. Ching, Role of Interatomic Bonding in the Mechanical Anisotropy and Interlayer Cohesion of CSH Crystals, *Cem. Concr. Res.*, 2013, **52**, 123–130.

19 J. Li, W. Zhang and P. J. M. Monteiro, Structure and Intrinsic Mechanical Properties of Nanocrystalline Calcium Silicate Hydrate, *ACS Sustainable Chem. Eng.*, 2020, **8**(33), 12453–12461.

20 J. Gao, X. Wu and S. Qin, The crystal chemistry and the compressibility of silicate-carbonate minerals: spurrite, galuskinite and tilleyite, *Geosci. Front.*, 2015, **6**(5), 771–777.

21 I. G. Richardson, The Calcium Silicate Hydrates, *Cem. Concr. Res.*, 2008, **38**(2), 137–158.

22 Y. Wu, X. Pan, Q. Li and H. Yu, Crystallization and Phase Transition of Tobermorite Synthesized by Hydrothermal Reaction from Dicalcium Silicate, *Int. J. Appl. Ceram. Technol.*, 2020, **17**(3), 1213–1223.

23 I. V. Pekov, N. V. Zubkova, N. V. Chukanov, V. O. Yapaskurt, S. N. Britvin, A. V. Kasatkin and D. Y. Pushcharovsky, Oyelite: New Mineralogical Data, Crystal Structure Model and Refined Formula $Ca_5BSi_4O_{13}(OH)_3 \cdot 4H_2O$, *East. J. Med.*, 2019, **31**(3), 595–608.

24 S. Huang, Z. Wang, F. Wang, F. Liu and M. Barati, Heat Transfer Properties and Molecular Mechanisms of Cuspidine ($Ca_4Si_2O_7F_2$): An Atomic-Scale Molecular Dynamics Study, *Chem. Eng. Sci.*, 2022, **253**, 117594.

25 R. A. Assaggaf, L. Alhajji, S. Siddique and S. K. Adekunle, Accelerated Carbonation Curing of Building Mortars Incorporating Volcanic Ash and Brine Sludge, *Constr. Build. Mater.*, 2024, **438**, 137267.

26 E. V. Galuskin, B. Lazic, T. Armbruster, I. O. Galuskina, N. N. Pertsev, V. M. Gazeev, R. Włodyka, M. Dulski, P. Dzierżanowski, A. E. Zadov and L. S. Dubrovinsky, Edgrewite $Ca_9(SiO_4)_4F_2$-Hydroxyledgrewite $Ca_9(SiO_4)_4(OH)_2$, a New Series of Calcium Humite-Group Minerals from Altered Xenoliths in the Ignimbrite of Upper Chegem Caldera, Northern Caucasus, Kabardino-Balkaria, Russia, *Am. Mineral.*, 2012, **97**(11–12), 1998–2006.

27 E. V. Galuskin, V. M. Gazeev, B. Lazic, T. Armbruster, I. O. Galuskina, A. E. Zadov, N. N. Pertsev, R. Wrzalik, P. Dzierżanowski, A. G. Gurbanov and G. Bzowska, Chegemite $Ca_7(SiO_4)_3(OH)_2$ a New Humite-Group Calcium Mineral from the Northern Caucasus, Kabardino-Balkaria, Russia, *Eur. J. Mineral.*, 2009, 1045–1059.

28 T. Armbruster, B. Lazic, I. O. Galuskina, E. V. Galuskin, E. Gnos, K. M. Marzec and V. M. Gazeev, Trabzonite, $Ca_4[Si_3O_9(OH)]OH$: Crystal Structure, Revised Formula, New Occurrence and Relation to Killalaite, *Mineral. Mag.*, 2012, **76**(3), 455–472.

29 G. Kresse and J. Furthmüller, Efficient Iterative Schemes for Ab Initio Total-Energy Calculations Using a Plane-Wave Basis Set, *Phys. Rev. B:Condens. Matter Mater. Phys.*, 1996, **54**(16), 11169–11186.

30 G. Kresse and J. Hafner, *Ab Initio* Molecular Dynamics for Liquid Metals, *Phys. Rev. B:Condens. Matter Mater. Phys.*, 1993, **47**(1), 558–561.

31 J. P. Perdew, K. Burke and M. Ernzerhof, Generalized Gradient Approximation Made Simple, *Phys. Rev. Lett.*, 1996, **77**(18), 3865–3868.

32 P. E. Blöchl, Projector Augmented-Wave Method, *Phys. Rev. B:Condens. Matter Mater. Phys.*, 1994, **50**(24), 17953–17979.

33 S. Grimme, J. Antony, S. Ehrlich and H. Krieg, A Consistent and Accurate Ab Initio Parametrization of Density Functional Dispersion Correction (DFT-D) for the 94 Elements H-Pu, *J. Chem. Phys.*, 2010, **132**(15), 154104.

34 H. J. Monkhorst and J. D. Pack, Special Points for Brillouin-Zone Integrations, *Phys. Rev. B:Condens. Matter Mater. Phys.*, 1976, **13**(12), 5188–5192.

35 W. Setyawan and S. Curtarolo, High-Throughput Electronic Band Structure Calculations: Challenges and Tools, *Comput. Mater. Sci.*, 2010, **49**(2), 299–312.

36 W.-Y. Ching and P. Rulis, *Electronic Structure Methods for Complex Materials: the Orthogonalized Linear Combination of Atomic Orbitals*, Oxford University Press, 2012.

37 W. Y. Ching, Theoretical Studies of the Electronic Properties of Ceramic Materials, *J. Am. Ceram. Soc.*, 1990, **73**(11), 3135–3160.

38 C. Biagioni, S. Merlino and E. Bonaccorsi, The Tobermorite Supergroup: A New Nomenclature, *Mineral. Mag.*, 2015, **79**(2), 485–495.

39 F. Mouhat and F.-X. Coudert, Necessary and Sufficient Elastic Stability Conditions in Various Crystal Systems, *Phys. Rev. B:Condens. Matter Mater. Phys.*, 2014, **90**(22), 224104.

40 C. Dharmawardhana, M. Bakare, A. Misra and W. Ching, Nature of Interatomic Bonding in Controlling the Mechanical Properties of Calcium Silicate Hydrates, *J. Am. Ceram. Soc.*, 2016, **99**(6), 2120–2130.

41 H. Manzano, J. S. Dolado, A. Guerrero and A. Ayuela, Mechanical Properties of Crystalline Calcium-silicate-hydrates: Comparison with Cementitious C-S-H Gels, *Phys. Status Solidi A*, 2007, **204**(6), 1775–1780.

42 N.-H. Hoang, D. T. Ha and T. T. Trinh, A First-Principles Insight into Thermodynamic and Mechanical Properties of

Xonotlite and Wollastonite Phases of High Temperature Geothermal Well Cement, *Results Mater.*, 2023, **20**, 100454.

43 S. J. Edrees, M. M. Shukur and M. M. Obeid, First-Principle Analysis of the Structural, Mechanical, Optical and Electronic Properties of Wollastonite Monoclinic Polymorph, *Comput. Condens. Matter*, 2018, **14**, 20–26.

44 D. Santamaria-Perez, J. Ruiz-Fuertes, T. Marqueño, J. Pellicer-Porres, R. Chulia-Jordan, S. MacLeod and C. Popescu, Structural Behavior of Natural Silicate–Carbonate Spurrite Mineral, $Ca_5(SiO_4)_2(CO_3)$, under High-Pressure, High-Temperature Conditions, *Inorg. Chem.*, 2018, **57**(1), 98–105.

45 M. F. Ashby, Chapter 3 – Engineering Materials and Their Properties, in *Materials Selection in Mechanical Design*, ed. Ashby, M. F., Butterworth-Heinemann, Oxford, 4th edn, 2011, pp. 31–56.